Corrugated surface for polymerase chain reaction (PCR) process: Thermal Rayleigh-Benard instability

Omar Rahli, Najwa Mimouni, Rachid Bennacer

To cite this version:

Omar Rahli, Najwa Mimouni, Rachid Bennacer. Corrugated surface for polymerase chain reaction (PCR) process: Thermal Rayleigh-Benard instability. International Journal of Thermal Sciences, 2021, 170, pp.107099. 10.1016/j.ijthermalsci.2021.107099 . hal-04274369

HAL Id: hal-04274369
https://cnrs.hal.science/hal-04274369

Submitted on 22 Jul 2024

Version of Record: https://www.sciencedirect.com/science/article/pii/S1290072921002611
Manuscript_0e61fd5efc09146336c89bd21c73fcd2

Corrugated surface for Polymerase chain reaction (PCR) process : Thermal Rayleigh-Benard instability

Omar Rahli [a], Najwa Mimouni [a, b], Rachid Bennacer [b,c*]

[a] LTPMP Laboratory. Faculty of Mech. and Proceeding Eng., Univ. of Sciences and Technology Houari Boumediene, Algiers, Algeria

[b] Tianjin Key Lab of Refrigeration Technology,
Tianjin University of Commerce, P.R.C.,300134.

[c] LMT, ENS Paris-Saclay, CNRS, Université Paris-Saclay,
4 avenue des Sciences, 91190 Gif sur Yvette, France
*Email : rachid.bennacer@ens-paris-saclay.fr

Abstract

Numerical investigation is performed to analyze natural convection heat transfer characteristics within a corrugated surface enclosure filled with fluid under the Rayleigh-Bénard (RB) instability. The impact of the geometric contribution associated with the convective RB effect, is analyzed to provide qualitative heat transfer and flow structure. Such thermal process is applying for improving the engineering Polymerase chain reaction (PCR) process to amplify a target DNA sample. The grid generation is used to transform the physical complex domain to a computational regular coordinate. The governing differential equations are discretized by Finite volume approach using a quadratic scheme approximation. The main objective of this work is to analyze the combined physical and geometric effects characterizing the corrugated enclosure, on the behavior of convective flow and to enlarge the active isothermal area favorable for the elementary process actions. Under the effect of the different control parameters defined by the dimensionless mathematical model, we demonstrate the existence of critical corrugations amplitude as a function of Ra-λ, describing the bifurcation from monocellular towards a bicellular flow. The active isothermal zone are identified, quantified and physical explanation and predictive expression were established.

Keywords: Corrugated cavity, Rayleigh-Benard convection, Heat transfer, CFD, Polymerase chain reaction (PCR).

1. Introduction

In the current global energy context, an understanding of the physical phenomena that occur in various industrial processes is necessary for optimizing energy consumption. Natural convection heat transfer and fluid flow in irregular closed cavities is one of the most studied thermal phenomena that has considerable attention of engineers because of its potential for improving heat transfer performance in reliable process. It is also of great importance in several thermal engineering applications such as electronic components cooling, micro-electromechanical systems (MEMS), heat exchangers, solar energy collectors, cold storage performance, building thermal insulation, nuclear energy and molecular biology process where the convective Polymerase chain reaction (**CPCR**) is one of the important tools.

The change and the location of surface waviness are considered as controlling parameters for optimizing the flow and thermal field characteristics. Frequently surfaces are intentionally roughened to enhance heat transfer.

A special case of thermal convection is the Rayleigh-Bénard (**RB**) convection; which corresponds to the situation of heating from the bottom and cooled from the top. The stratified and stable state, becomes unstable above critical situation. A density gradient is generated by the temperature difference between the two active walls. This driving force is opposed to two other braking forces, which are viscous dissipation and heat dissipation. This relationship between gravitational driving forces and resistant forces is defined by the Rayleigh number, which must exceed a certain critical value for the birth of convection. Due to such strong nonlinear coupling and the low number of controlling parameters, RB convection has been the subject of several experimental and theoretical works. The importance of this phenomenon has given rise to several researches having for purpose of understanding and using it; in the framework of fundamental or applied engineering, this research admits extremely broad and interesting developments.

The study of this phenomenon in complex geometries was relatively limited because of the increase in the flow complexity. The present literature tries to review the previous studies involving the case of corrugated surfaces for the analysis of convection problems.

Varol and Oztop [1] have performed a numerical free convection heat transfer and fluid flow in a horizontal and shallow wavy enclosure. The bottom wall at hot temperature is varied with a sinusoidal function while the top flat wall is kept at a cold temperature. Their results indicated that heat transfer was decreased with increasing wavelength undulation, however, the exchange is favored with the increase Rayleigh number and enclosure aspect ratio.

Saha *et al.* [2] analyzed numerically fluid flow in inclined enclosure with vertical wall of sinusoidal shape maintained at a constant low temperature and a constant heat flux source discretely embedded at the bottom wall. It is concluded that the average Nusselt number increases as inclination angle increases for different heat source sizes. For free convection in an enclosure with vertical wavy walls, Mahmud *et al.* [3] shown the effect of aspect ratio, surface waviness on heat transfer at different Grashof numbers. Authors observe at low aspect ratios and selected Grashof numbers, a significant increase in heat transfer. Das and Mahmud [4] investigated thermal and hydrodynamic fluid flow within wavy horizontals walls enclosure. Convective analysis showed that amplitude-wavelength ratio has no significant influence on average heat transfer. They demonstrate that natural convection heat transfer is considerably influenced by the aspect ratio variations. In addition, the heat transfer irreversibility was measured [5]. Favier *et al.* [6] study the evolution of a melting front between the solid and liquid phases for of a pure incompressible material driven by unstable RB convection. The authors shown for very thin fluid layer, that convective flow appear as the effective Rayleigh number increases.

Rayleigh-Bénard convection instabilities in L shape and diagonally flipped-L shape enclosures are studied by Gawas and Patil [7], using LBM-MRT. This unsteady flow behavior is characterized by using time-dependency signal of averaged Nusselt number and its corresponding frequency analysis. Geometry Optimization is then carried out to obtain the best heat transfer rate.

Viscous flow of Newtonian fluid in two-dimensional enclosures, consisting of regular, square shaped, corrugations on the bottom wall is studied numerically by Bisht *et al* [8]. After comparing LBM and fictitious domain method (FDM) results, a flow features are presented for various Reynolds number and corrugations characteristics. This input parameters have a great effect on number of vortexes appeared inside the enclosure.

Convective flow induced by heating blocks periodically distributed on lower surface of a channel, is analyzed by Mouhtadi *et al.* [9]. The validity of the isothermal model under the multiple steady solutions obtained, is examined as a function of the different control parameters. The onset of longitudinal RB convective rolls in 3D configuration was analyzed by Rahli *et al.* [10]. The authors demonstrate that the dimensionless length of fully developed secondary flow is strongly influenced by the cooperating or opposed buoyancy forces.

Adjlout *et al.* [11] have investigated laminar convective flow in inclined wavy wall cavity heated differentially. Simulations were performed for different inclination angles, amplitudes and Rayleigh numbers; one of their interesting results was a decrease of averaged heat transfer compared to regular square cavity. So, they recommended investigating the hot wall geometry optimization.

Biswal and Basak [12] investigate the role of differential *vs.* RB heating at enclosures involving curved walls for efficient processing via entropy generation approach. They show for noncurved walls that magnitudes of entropy generation and average heat transfer are significantly lesser for the RB heating. However, for the concave or convex cases, the optimal configuration is strongly controlled by the modified Darcy and Prandtl numbers. Using scale analysis, Choukairy *et al.* [13] present interesting correlations to quantify the heat exchanges as a function of the heated wall thickness.

Free convection inside a vertical cosine curved walls cavity is numerically investigated by Misirlioglu *et al.* [14]. The results indicate that for large modified Rayleigh values, aspect ratio under 3 and surface waviness about 0.5, the local Nusselt number may become negative; which means the generated heat cannot be transferred through the domain.

Two-dimensional steady state natural convective flow in a square inclined enclosure with vertical vee-corrugated isothermal sidewalls has been numerically studied by Hussain *et al.* [12, 15]. A discrete heat flux is flush-mounted on the bottom wall. The authors demonstrate that inclination angle strongly affect the convective flow.

An analysis of thermal performance in lid driven wavy enclosure with various configurations is presented by Chattopadhyay *et al.* [16]. One of the straight walls is no uniformly heated, while all other are maintained at cold temperature. They present the effects of different dimensionless parameters on fluid flow pattern and Nusselt’s numbers evolutions. The most important results presented are mentioned that the fluid flow is highly influenced by the direction of moving wall and the vortex structures are strongly changed from configuration to another one. The entropy generation increase linearly with decreasing Richardson number.

Moreover, these classical studies dealing with heat transfer enhancement, another very interesting applications linking thermal natural convection induced by RB effect to the molecular biology process is the Polymerase chain reaction (**PCR**). This recently developed process is adopted in several fields, such as biomedicine, animal and plant science and food safety [17-21]. The efficiency and improvement of this technology has been during this last decade, one of the major challenges of the scientific community given its important diagnosis.

Thus, the execution of this process under the effect of natural convection of thermal origin has already shown its effectiveness in improving the results obtained for PCR process [19] or for cryosurgery within the biological tissue, by controlling the cooling/thawing rate over some critical range of temperatures and freezing states [22]. Indeed, the convective motion will ensure a continuous flow, and consequently an ideal thermal cycle, without having recourse to an external agent, as demonstrated by Chen and Hsieh [23] using infrared (IR) heating. A comprehensive experiments of measuring temperature profiles versus operational and geometrical parameters are presented.

PCR is powerful technology whose role is to amplify a target DNA sample; the process is carried out in three repetitive recycling stages at different temperatures. These stages, see Fig. 1, are the denaturation step at high temperature (95°C), annealing step, at low temperature (50–60°C) and the extension stage at moderate temperature (72–77°C) [24]. The problem with conventional PCR thermal cyclers lies in the ability to control these temperatures precisely, which increases cycle times and reduces the efficiency of ensuring optimal amplification. [19]. Therefore, natural convective PCR (**CPCR**) under RB effects (**RB-PCR**) is one of the potential approaches to overcome these limitations, by ensuring a continuous flow which will allow to execute the three stages of the protocol continuously, while controlling the degrees of temperatures suitable for better amplification. Thus, the upward and downward motion of fluid particles induced by buoyancy-driven instability, will continuously entrain the reagents which will be transported from the hot zones to the cold ones executing the different phases of the process. A schematic representation is presented in figure 1 illustrating the operating principle. This PCR in natural convection systems was previously presented by Yariv *et al.* [25], using the original RB-cell configuration. The beneficial contribution to the overall amplification process by molecular diffusion has been demonstrated.

The first research teams to use thermal convection mode of CPCR, are Benett *et al.* [26] for closed-loop, and Hwang *et al.* [27], performed in a cylindrical capillary tube heated from the bottom. The geometrical and material characteristics for closed enclosures design distinguished at the CPCR remain a major challenge to improve the efficiency of these processes. To date, several forms have been proposed, rectangular, triangular or planes. For the RB-CPRC, the major part of the proposed studies considers capillary tubes or enclosures with square geometry, under the laminar flow hypothesis [24, 25, 28]. More details and information on the subject are exposed in the exhaustive bibliographical review carried out by

Miao *et al.* [19]. It should be noted that it has been shown that the adoption of RB convection in stationary mode with single-cell regime, is the most suitable for the PCR reaction [25]. However, this configuration is subject to major criticism due to the weakening flow intensity outside the vortex relatively to the internal zones, following the non-slip conditions on the rigid walls. Thus, the braking flow will necessarily increase the time cycle, especially in the vicinity of the walls. The effectiveness of this type of configuration in PCR, is only significant over a selected streamlines range ($\Psi_{Max} >> \Delta\Psi_{eff} >> \Psi_{Min}$). To remedy this constraint, we propose to modify the flow structure, under the geometric deformation effect, with an optimal corrugation amplitude, which will favor the flow intensity and modify the temperature distribution fields in the enclosure. This configuration will allow us to make the best use of the upward motion particles zone, until then untapped for the PCR cycle. On the other hand, the bifurcation towards bicellular convective mode can improve the efficiency of PCR by modifying the convective flow intensity and thus reduce the operation time cycle, or to double the number of execution PCR stages sites.

It is in this context of the geometric shape of the cavity that our orientation towards this type of application (RB-PCR) fits. Because, to our knowledge, during our analysis of the bibliographic review, the corrugated cavities had never been treated in PCR procedures. In fact, the use of a cavity with a corrugated lower wall, depending on its characteristics (wave amplitude and number of waves), will completely modify the convective flow structures as well as the thermal gradients, which will strongly influence the execution time of the different stages of the PCR process, and reduce the time cycle allowing the DNA sample to be amplified as best as possible.

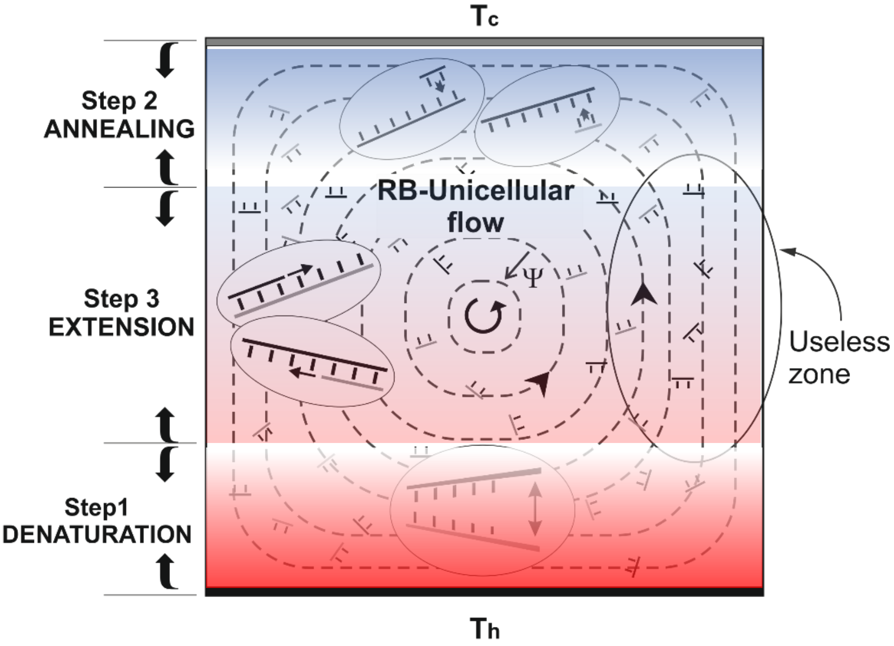

Fig. 1. Schematic PCR in a Unicellular Rayleigh-Benard flow [25].

Even our present work remains exclusively thermodynamic nature, we try by the convective flow prediction analysis, to bring a better understanding which can provide light ideas for the scientific community specialized in the field of PCR to develop new efficient DNA amplification systems.

The main propose of this work is to examine the momentum and energy transport processes in a square enclosure filled with fluid with a wavy bottom surface. The problem phenomena are treated under the classical RB convection mode. The cavity is sustained under a vertical temperature gradient by subjecting the bottom wall to a relatively higher temperature than the top. The results are shown in terms of parametric presentations of streamlines and isotherms for various considered pertinent dimensionless parameters. These dimensionless groups include the Rayleigh number, the corrugation amplitude and the wavy surface undulations number. Finally, the implications of the above dimensionless parameters are also depicted on the local and average Nusselt number predictions.

2. Modeling and governing equations

The problem under consideration is a two-dimensional square (H x H) wavy enclosure fully filled with a binary fluid, as shown in Fig. 2. The convective mode considered is the classical RB phenomenon; where the cavity is heated from below, on its corrugated surface, by a temperature T_h and cooled from above on the rectilinear surface by a temperature T_c. The vertical walls are assumed adiabatic.

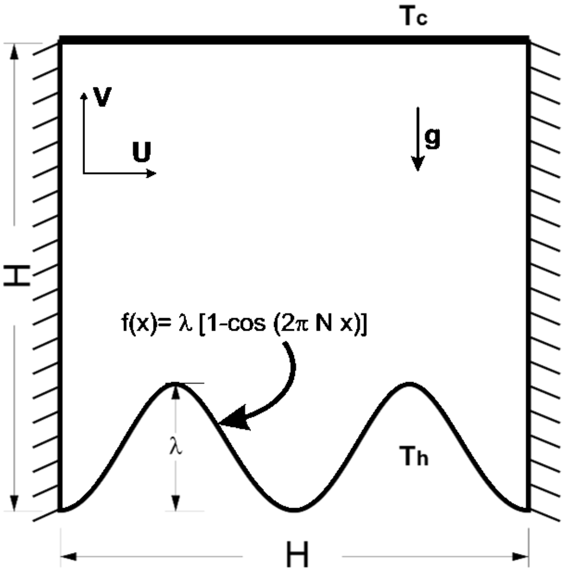

Fig. 2: Physical model

The fluid saturating the porous substrate is considered incompressible and Newtonian with Prandtl number kept constant. The fluid properties are also assumed constant except for the density variation which is treated according to Boussinesq approximation while viscous dissipation effects are considered negligible. The viscous laminar incompressible flow and the temperature distribution inside the cavity are described by mean of the Darcy-Brinkman model and the energy equation, respectively. In performing simulations, the profile of the wavy-wall was modeled as follows:

$$f(x) = \lambda\,[1 - (\cos(2\pi\, N\, x)] \tag{1}$$

The governing differential equations of the mass continuity, momentum and energy can be written in dimensionless form using the following dimensionless variables:

$$X = \frac{x}{H};\quad Y = \frac{y}{H};\quad U = \frac{u\,H}{a};\quad V = \frac{v\,H}{a};\quad \theta = \frac{T-Tc}{Th-Tc}\;;\quad P = \frac{p-p_0}{\rho_0\left(\frac{a}{H}\right)^2} \tag{2}$$

The dimensionless governing continuity equation, x- and y-momentum equations, and energy equation can then be written respectively as:

$$\frac{\partial U}{\partial X} + \frac{\partial V}{\partial Y} = 0 \tag{3}$$

$$\left(\frac{\partial(\mathrm{U\,U})}{\partial \mathrm{X}}+\frac{\partial(\mathrm{U\,V})}{\partial \mathrm{Y}}\right)=-\frac{\partial \mathrm{P}}{\partial \mathrm{X}}+\ \mathrm{Pr}\left[\frac{\partial^2\mathrm{U}}{\partial \mathrm{X}^2}+\frac{\partial^2\mathrm{U}}{\partial \mathrm{Y}^2}\right] \tag{4}$$

$$\left(\frac{\partial(\mathrm{U\,V})}{\partial \mathrm{X}}+\frac{\partial(\mathrm{V\,V})}{\partial \mathrm{Y}}\right)=-\frac{\partial \mathrm{P}}{\partial \mathrm{Y}}+\mathrm{Pr}\left[\frac{\partial^2\mathrm{V}}{\partial \mathrm{X}^2}+\frac{\partial^2\mathrm{V}}{\partial \mathrm{Y}^2}\right]+Ra\,Pr\,\theta \tag{5}$$

$$\frac{\partial(\mathrm{U}\theta)}{\partial \mathrm{X}}+\frac{\partial(\mathrm{V}\theta)}{\partial \mathrm{Y}}=\left[\frac{\partial^2\theta}{\partial \mathrm{X}^2}+\frac{\partial^2\theta}{\partial \mathrm{Y}^2}\right] \tag{6}$$

where, Ra is the thermal Rayleigh number and Pr the Prandtl number. The parameters g, β, ν and a refer to the gravitational acceleration, expansion coefficient, kinematic viscosity and thermal diffusivity, respectively.

$$Pr=\nu/\mathrm{a}\ ,\ Ra=\frac{\mathrm{g}\,\beta_{\mathrm{T}}\,\Delta\mathrm{T}\,\mathrm{H}^3}{\nu\ \mathrm{a}}\ ,\ \mathrm{a}=\frac{\mathrm{k}}{\rho\mathrm{C_p}} \tag{7}$$

In the case of complex geometry, the problem of grid generation remains one of the great difficulties. To overcome this constraint, we often use a transformation of coordinates from the physical domain to a fictitious domain, called computational domain, which will serve as computation space ([29-31]).

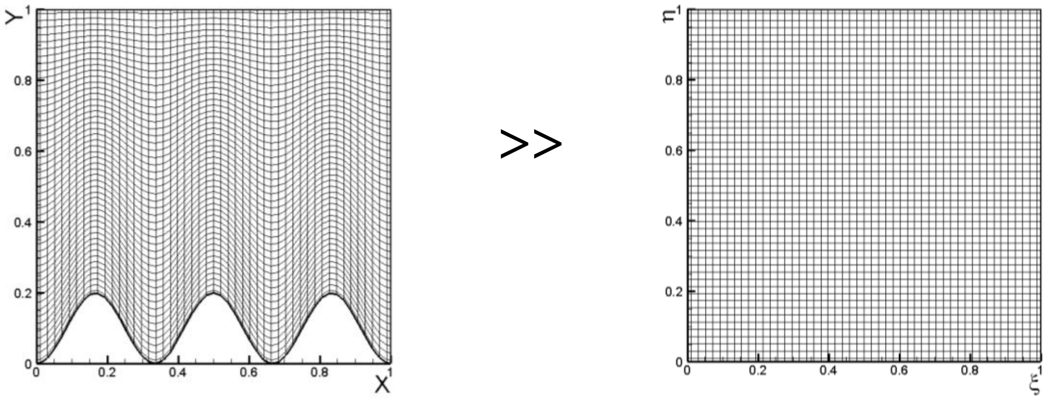

$g(X,Y)$ $g(\xi,\eta)$

Fig. 3: Physical domain and transformed computational domain

If the physical domain is described using the variables X and Y, and the computational domain is described using the coordinates ξ and η, the general continuous transformation from the physical domain to the computational domain shown in Fig. 3 can be written as:

$$\xi=\ \xi(\mathrm{X},\mathrm{Y}) \tag{8}$$

$$\eta=\eta(\mathrm{X},\mathrm{Y}) \tag{9}$$

In many applications, the coordinate transformations are given numerically, then the metrics are calculated by finite differences. In our case the transformation metrics are given by:

$$\frac{\partial f}{\partial X} = \xi_X \frac{\partial f}{\partial \xi} + \eta_X \frac{\partial f}{\partial \eta} \tag{10}$$

$$\frac{\partial f}{\partial Y} = \xi_Y \frac{\partial f}{\partial \xi} + \eta_Y \frac{\partial f}{\partial \eta} \tag{11}$$

$$\begin{aligned}\frac{\partial^2 f}{\partial X^2} = {} & J^2\left({Y_\eta}^2 f_{\xi\xi} - 2\, Y_\xi Y_\eta f_{\xi\eta} + {Y_\xi}^2 f_{\eta\eta}\right) \\ & + J^3\left({Y_\eta}^2 y_{\xi\xi} - 2Y_\eta Y_\xi Y_{\xi\eta} + {Y_\xi}^2 Y_{\eta\eta}\right)\left(Xf_{\xi} {}_- X_\xi f_\eta\right) \\ & - \left({Y_\eta}^2 X_{\xi\xi} - 2Y_\eta Y_\xi Y_{\xi\eta} + {Y_\xi}^2 X_{\eta\eta}\right)\left(Y_\xi f_{\eta} {}_- Y_\eta f_\xi\right)\end{aligned} \tag{12}$$

$$\begin{aligned}\frac{\partial^2 f}{\partial Y^2} = {} & J^2\left({X_\eta}^2 f_{\xi\xi} - 2\, X_\xi X_\eta f_{\xi\eta} + {X_\xi}^2 f_{\eta\eta}\right) \\ & + J^3\left({X_\eta}^2\, Y_{\xi\xi} - 2X_\xi X_\eta Y_{\xi\eta} + {X_\xi}^2 Y_{\eta\eta}\right)\left(X_\eta f_{\xi} {}_- X_\xi f_\eta\right) \\ & - \left({X_\eta}^2 X_{\xi\xi} - 2X_\eta X_\xi X_{\xi\eta} + {X_\xi}^2 X_{\eta\eta}\right)\left(Y_\xi f_{\eta} {}_- Y_\eta f_\xi\right)\end{aligned} \tag{13}$$

Where J denotes the Jacobian of the transformation:

$$J = \frac{1}{X_\xi Y_\eta - Y_\xi X_\eta} \tag{14}$$

Using this approach, the transformed governing continuity equation, x- and y-momentum equations, and energy equation can then be written respectively as follow:

$$\frac{\partial U^c}{\partial \xi} + \frac{\partial V^c}{\partial \eta} = 0 \tag{15}$$

$$\begin{aligned}&\left(\frac{\partial (U^c\, U)}{\partial \xi} + \frac{\partial (V^c\, U)}{\partial \eta}\right) = -\left(f_{11}\frac{\partial P}{\partial \xi} + f_{21}\frac{\partial P}{\partial \eta}\right) + Pr\left[\frac{\partial}{\partial \xi}\left(q_{11} J\frac{\partial U}{\partial \xi}\right) + \frac{\partial}{\partial \eta}\left(q_{12} J\frac{\partial U}{\partial \xi}\right) + \right. \\ &\left. \frac{\partial}{\partial \xi}\left(q_{12} J\frac{\partial U}{\partial \eta}\right) + \frac{\partial}{\partial \xi}\left(q_{22} J\frac{\partial U}{\partial \eta}\right)\right]\end{aligned} \tag{16}$$

$$\begin{aligned}&\left(\frac{\partial (U^c\, V)}{\partial \xi} + \frac{\partial (V^c\, V)}{\partial \eta}\right) = -\left(f_{11}\frac{\partial P}{\partial \xi} + f_{21}\frac{\partial P}{\partial \eta}\right) + Pr\left[\frac{\partial}{\partial \xi}\left(q_{11} J\frac{\partial V}{\partial \xi}\right) + \frac{\partial}{\partial \eta}\left(q_{12} J\frac{\partial V}{\partial \xi}\right) + \right. \\ &\left. \frac{\partial}{\partial \xi}\left(q_{12} J\frac{\partial V}{\partial \eta}\right) + \frac{\partial}{\partial \eta}\left(q_{22} J\frac{\partial V}{\partial \eta}\right)\right] + \frac{Ra.Pr.\theta}{J}\end{aligned} \tag{17}$$

$$\left(\frac{\partial (U^c\, \theta)}{\partial \xi} + \frac{\partial (V^c\, \theta)}{\partial \eta}\right) = \left[\frac{\partial}{\partial \xi}\left(q_{11} J\frac{\partial \theta}{\partial \xi}\right) + \frac{\partial}{\partial \eta}\left(q_{12} J\frac{\partial \theta}{\partial \xi}\right) + \frac{\partial}{\partial \xi}\left(q_{12} J\frac{\partial \theta}{\partial \eta}\right) + \frac{\partial}{\partial \xi}\left(q_{22} J\frac{\partial \theta}{\partial \eta}\right)\right] \tag{18}$$

Where:

$$f_{11} = Y_\eta \;\; , \;\; f_{12} = -X_\eta \, , \;\; f_{21} = -Y_\xi \;\; , \;\; f_{22} = X_\xi$$

$$q_{11} = (f_{11}^2 + f_{12}^2),\ q_{22} = (f_{21}^2 + f_{22}^2),\ q_{12} = (f_{11}f_{21} + f_{12}f_{22})$$
$$U^c = Y_\eta U - X_\eta V = f_{11}U + f_{12}V$$
$$V^c = X_\xi V - Y_\xi U = f_{22}V + f_{21}U$$

In non-dimensional form, the following boundary conditions for the velocity components and temperature are imposed for motion and energy conservation equations.

$$\text{For } 0 < \xi < 1 \quad \begin{cases} \eta = 0 \rightarrow U, V = 0 \ \text{ and } \ \theta = 1 \\ \eta = 1 \rightarrow U, V = 0 \ \text{ and } \ \theta = 0 \end{cases} \tag{19}$$

$$\text{For } 0 < \eta < 1 \quad \begin{cases} \xi = 0 \rightarrow U, V = 0 \ \text{ and } \ \left.\frac{\partial\theta}{\partial\xi}\right| = 0 \\ \xi = 1 \rightarrow U, V = 0 \ \text{ and } \ \left.\frac{\partial\theta}{\partial\xi}\right| = 0 \end{cases} \tag{20}$$

The local Nusselt number *Nu* is expressed as:

$$Nu_L = -\partial\theta/(\partial\hat{n}) \tag{21}$$

While the average Nusselt number Nu_{Av} is obtained by integrating the local Nusselt number along the bottom wavy surface and is defined by:

$$Nu_{AV} = \frac{1}{S}\int_0^S Nu \ ds \tag{22}$$

$$S = \int_0^1 \sqrt{1 + \left(\frac{dY}{dX}\right)^2}\, dX \tag{23}$$

Where S is the total curve length of the wavy surface.

3. Numerical method

The governing equations are discretized using a finite volume method with SIMPLER algorithm [32] to handle coupling between the momentum and continuity equations. Third order QUICK scheme [33] is used in approximating the advection terms. The discretized algebraic equations were solved by means of the combined method, line by line, based on the combination between the TDMA direct method and Gauss-Seidel iterative procedure. Denser grid clustering distribution near the boundaries of 121x121 nodes are used.

To ensure convergence of the solution procedure, the following criteria are applied to all dependent variables over the solution domain:

$$\frac{\sum\left|\phi_{ij}^{m}-\phi_{ij}^{m-1}\right|}{\sum\left|\phi_{ij}^{m}\right|} \leq 10^{-5} \qquad (24)$$

where ϕ represents a dependent variable, *i.e.* U, V, P and θ, the subscripts i, j indicates a grid point and the superscript m the current iteration. Under relaxation factors of 0.2 and 0.9 were applied to U, V and θ, respectively.

4. Results and discussions

Before proceeding to the parameterized study and numerical simulations, it is necessary to demonstrate that our computer code used is capable of reproducing results already obtained by other work. This validation process consists of executing the numerical code under specific conditions for reference problems and then comparing the results obtained with data published in the literature.

In the case of a purely thermal natural convection in a square cavity in classical RB situation, Table.1 summarizes the values of the average Nusselt number (Nu_{Av}) obtained on the active horizontal wall, as a function of the intensity of the imposed thermal gradient, characterized by the thermal Rayleigh number. Our results obtained with our computer code are compared to those of reference [34] considered as a Benchmark of the physical problem studied. The values obtained show perfect agreement with those of the reference with a maximum error which does not exceed 1.5% recorded at $Ra = 10^{+6}$.

TABLE 1. Comparison of average Nusselt number with literature results.
(RB convection in square cavity)

Ra	Benchmark [34]	Present
10^{+3}	1.0004	**1.0004**
10^{+4}	2.1581	**2.1573**
10^{+5}	3.9103	**3.9011**
10^{+6}	6.3092	**6.3955**

The next section present results obtained by analyzing the effects of different parameters controlling the thermal convective RB phenomena on the corrugated cavity. The simulations are carried out for a Rayleigh number varying between $10^{+3} \leq Ra \leq 10^{+6}$. The geometric parameters of the corrugated surface will be analyzed as a function of the corrugation amplitude taken between 0.1 and 0.8. All the numerical predictions were obtained for square computational domain by using stagnant fluid as first guess solutions.

The present work is limited to a single ripple (N=1), where we present the simultaneous effect of the thermal forces, characterized by the *Ra* number, associated to the geometric deformation related to the corrugation amplitude λ. The effect of corrugations number N will be treated separately in next work, given the complexity of the convective flow induced by the increasing undulations number. The results are presented in terms of streamlines and isotherms in the considered domain.

For low Rayleigh number ($Ra=10^{+3}$) under the threshold for the appearance of convection (Ra_c = 1707.7), it can be seen, whatever the amplitude undulation (Fig.4), that the convective flow is relatively weak characterized by low velocity regime, bicellular, counter-rotating and symmetrical with respect to the line X = 0.5 as shown by streamlines of Fig. 4 (λ=0.1 and λ=0.6).

Isotherms present a stratification of the temperature with lines which are almost parallel to each other and follow the geometry of the corrugated surfaces, contrary to the case of non-deformed cavity. This behavior is due to the dominance of the conductive flow regime where the transfer of thermal agitation is carried out by microscopic transmission. The exchanges between the two walls will then be ineffective and of low intensity.

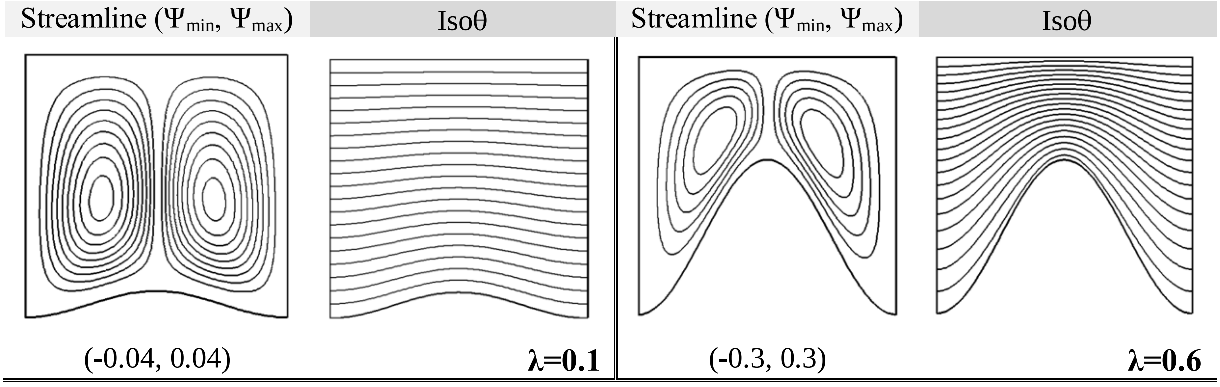

Fig. 4: Stream line (left) and Isotherms (Right), $Ra=10^{+3}$, N=1

The increase in the thermal force characterized by the Rayleigh number beyond the critical instability threshold ($Ra=10^{+4}$), generates the increase in the intensity of the flow and promotes the birth of the convective regime. Thus, the general situation is that of a fluid having an increasing density with altitude and thus manifesting a potential instability. The buoyancy caused by this difference in density tends to raise the lighter fluid and lower the heavier. This physical system thus couples a problem of mechanical stability (variation of density) with a problem of heat transfer (variation of temperature). If at a point a positive disturbance of the temperature gradient appears, Archimedes' buoyant force induces an upward movement of the fluid; this results a local convective supply of fluid particles coming from the hot lower layers; and vice versa in the case where the disturbance is negative. The upward or downward motion is then completely regular except for the fluid particles, which meet an interface, which obliges it to carry out a parallel trajectory to this interface despite to the mass conservation law.

At low amplitude undulation $\lambda \leq 0.2$, it can be seen in Fig. 5, that the convective flow gives rise to quasi-unicellular structures (with small secondary vortexes), dictated by a macroscopic thermal agitation transfer, and occupying almost the entire enclosure with counterclockwise circulation. This direction of flow can be reversed due to the multiplicity of physical involved phenomena or different initialization already demonstrated in the literature. The increase in the amplitude of the deformations from $\lambda = 0.1$ to $\lambda = 0.2$ favors the intensification of the flow shown by the limit values of the stream functions. In accordance with this natural convection flow, the isotherms present a distortion in harmony with the flow direction, which is more important than λ increases ($\lambda = 0.2$). These distortions cause the crushing of the thermal boundary layers at levels of the active walls; observed on the left side of the hot surface and on the right zone of the cold wall; this is obviously justified by the fluid flow direction. This convective transfer mode observed for $\lambda \leq 0.2$ generates a significant improvement in exchanges and increases the efficiency of the conductive microscopic transfer occurs at the walls.

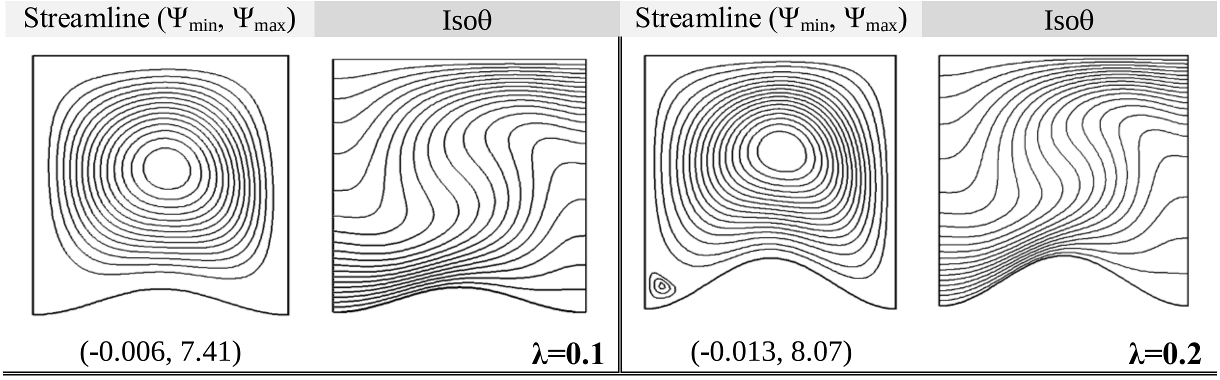

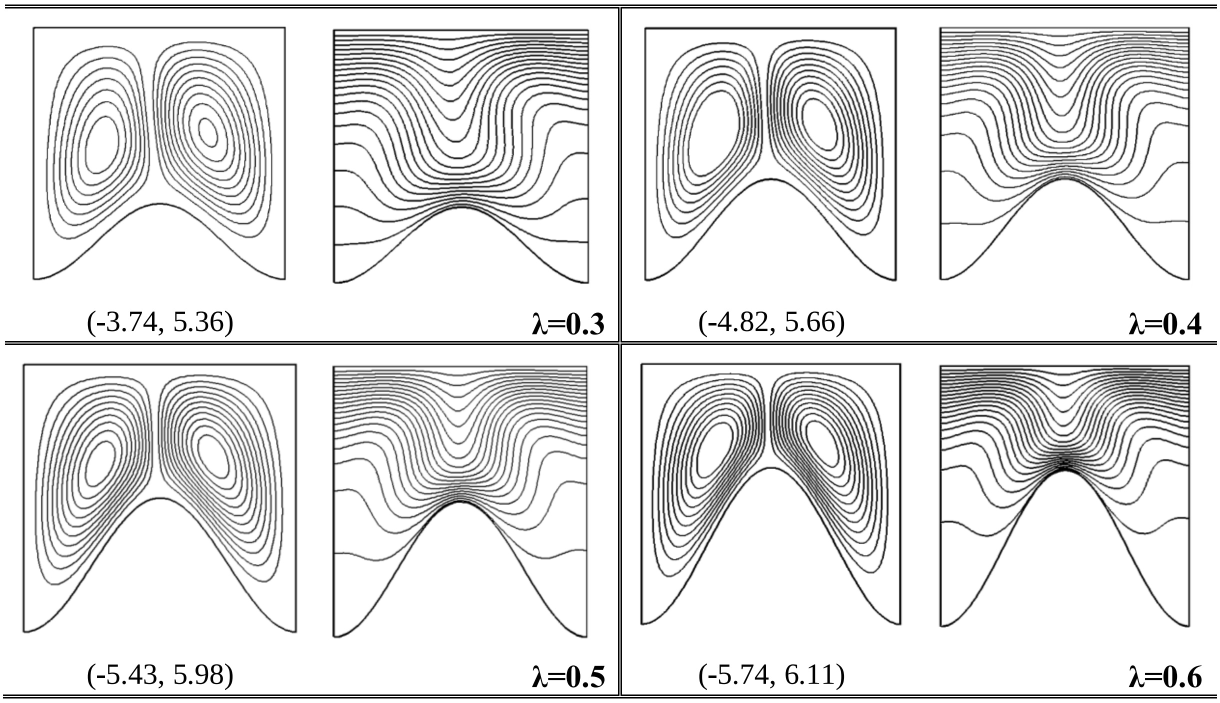

Fig. 5: Stream line (left) and Isotherms (Right), Ra=10^{+4}, N=1

As already indicated in the literature, the structures of RB convection, are strongly dependent on the physical and geometric characteristics of the system, and may not be established if the damping mechanisms that are, the conductivity thermal, linked to thermal disturbance, and viscosity, linked to dynamic disturbance, are very important. Indeed, we can show that these two energy diffusion mechanisms can modify the counter-rotating cells, in particular their sizes and wavelengths. In the case of strong temperature and speed gradients, the vortices formed allow strong diffusions of momentum and heat, which reduces motor imbalances and hinders the fluid motion. If the vortexes are very far apart, the parietal friction stress, linked to the horizontal particle motion at an interface, becomes more and more important and thus slowing down the movement.

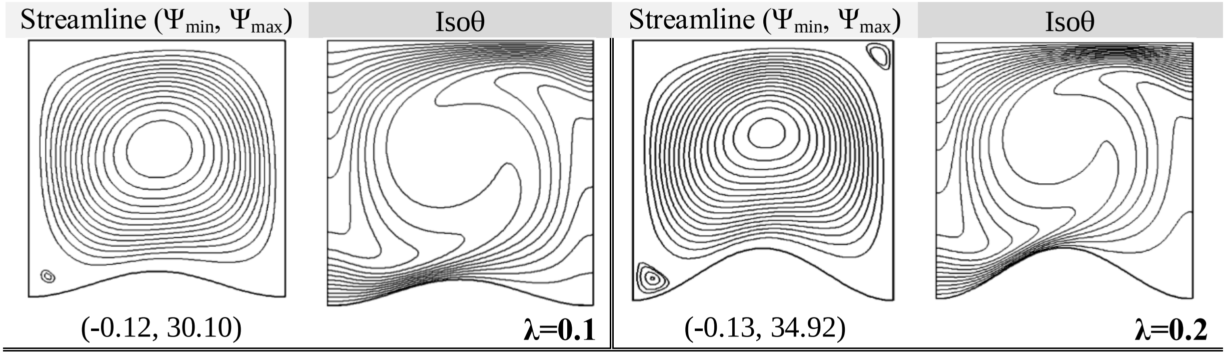

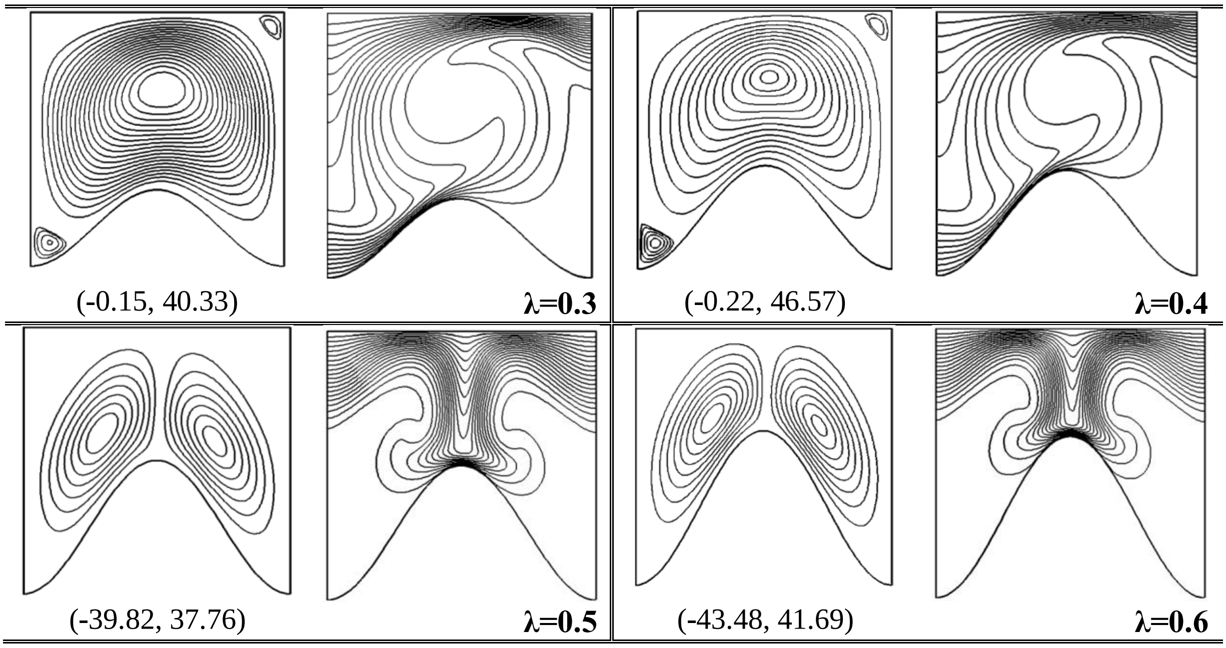

(-0.15, 40.33) **λ=0.3**

(-0.22, 46.57) **λ=0.4**

(-39.82, 37.76) **λ=0.5**

(-43.48, 41.69) **λ=0.6**

Fig. 6: Stream line (left) and Isotherms (Right), *Ra*=10^{+5}, N=1

It is in this context that we explain the flow structures obtained for λ≥0.3 (Fig.5), where we notice under the effect of the geometric deformation of the cavity, the formation of bicellular contra-rotative regime caused by the increase of corrugation amplitude, which forms a fictitious wall along the crest of the deformation (X = 0.5). This bi-cellular regime is almost symmetrical with respect to this fictitious wall, especially when the amplitude increases (λ=0.6). The horizontal movements of the fluid particles then end, when they meet this fictitious zone of separation, to start an upward or downward movement, depending on the direction of flow. When the fluid particles meet this fictitious zone of separation, their horizontal motion ends to start an upward or downward movement, depending on the flow direction. Thus, this fictitious zone will create a connection link, which gives a regular and self-organized overall motion characterized by the formation of counter-rotating cells.

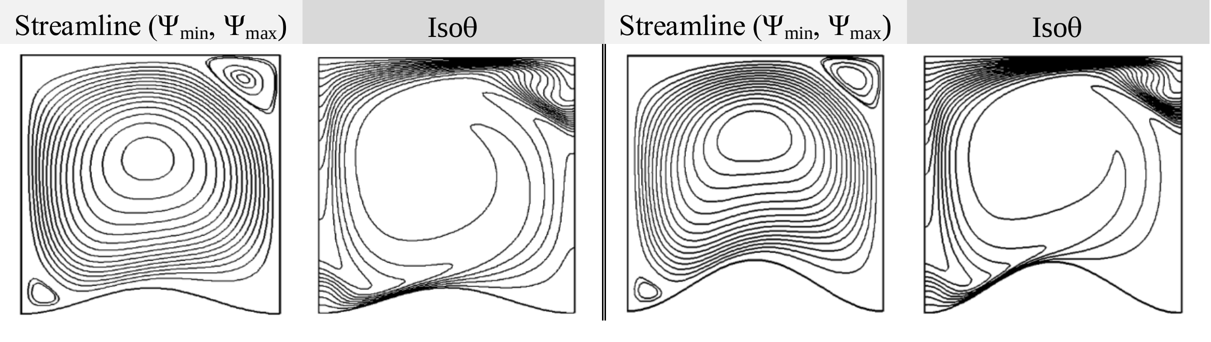

Streamline (Ψ_{min}, Ψ_{max}) Isoθ Streamline (Ψ_{min}, Ψ_{max}) Isoθ

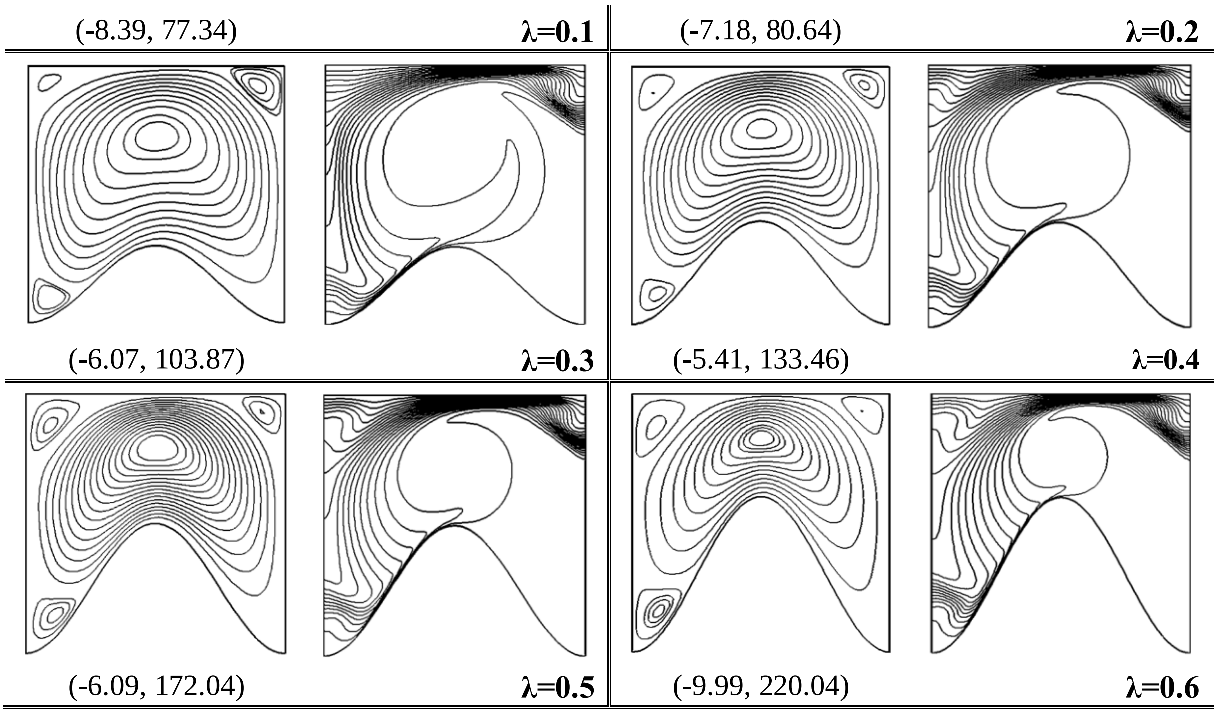

Fig. 7: Stream line (left) and Isotherms (Right), Ra=10^{+6}, N=1

Following the formation of the bicellular regime, the flow intensity was reduced from an amplitude of λ=0.2 to λ=0.3, which is probably due to the imbalance in the kinetics of the fluid particles. Beyond this value (λ>0.3), the inertia resumes its increase with the increase in the amplitude of undulation, following the aggravated confinement caused by these deformations.

In the case of the bicellular convective regime, the isotherms present quasi-symmetrical distortions relative to the center line X = 0.5; in accordance to the counter-rotating motion of the cells. This is causing the crushing of the thermal boundary layer on the hot wall, at the crest of the deformation, with increasing gradients; and a widening outside this zone, where it is observed that the compartments at the corners are isothermal, characterized by passive surface part to the heat transfer. This phenomenon is reversed on the cold wall.

By further increasing the thermal force (Ra=10^{+5}), we could really understand the interaction between the physical effects, due to the Rayleigh number, and those of geometric origin due to the deformation of the lower wall (Fig. 6). The physical phenomena observed remain in the same order of discussion, except that in this case, we note that the dominance of the quasi-unicellular regime persists until λ = 0.4, and the bifurcation towards a bicellular regime is not observed until λ = 0.5, where the geometric effects will prevail over the thermal forces, and thus impose the installation of the counter-convective regime as shown by streamlines of Fig. 7. It should be noted that following the intensification of the flow, the changes in the isotherms for $\lambda \leq 0.4$ illustrate the increase in the isothermal surface recorded in the right lower compartment of the cavity and thus reducing the active wall dimension which defines the conductive transfer at the lower hot border. This configuration will promote the denaturation in the RB-PCR application. Beyond an amplitude of 0.5, we note the accentuation of the geometric effect with a bicellular flow characterized by greater inertia, and bigger isothermal compartments ($\lambda = 0.6$).

For a higher Rayleigh number ($Ra=10^{+6}$), he geometric effect, for the chosen range of values, does not manage to dictate its dominance even at $\lambda = 0.6$ (Fig. 7); the convective flow remains dominated by the buoyancy forces, with a unicellular structure occupying almost the entire wavy cavity. The inertia zone is proportional to the increasing amplitude. However, it is important to report the existence of small cells at the corner enclosure, mainly due to the flow intensity. On the other hand, the isothermal surface due to the behavior of the thermal boundary layer, is as greater as λ increases; this will considerably affect the transfer rates and the exchange may not have a monotonous variation depending the amplitude. When the Rayleigh number is around 10^{+6}, our simulations allowed us to show that the bifurcation towards a bicellular flow is only observed up to an amplitude of 0.8, as shown in Fig. 8 representing the iso-values.

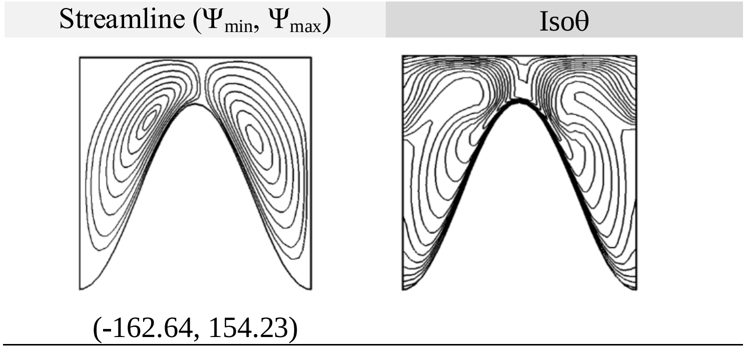

Fig. 8: Stream line (left) and Isotherms (Right), $Ra=10^{+6}$, N=1, $\lambda=0.8$

For the RB-PCR application, we can affirm from these visualizations that the use of a corrugated enclosure can improve the process of the DNA sample amplification. As an example, for $Ra = 10^{+6}$ case, it can be seen that the flow is clearly favored by the increasing corrugation amplitude. Nevertheless, it is necessary to determine the optimal amplitude which offers the favor flow intensity associated with a quasi-unicellular flow, where the intensity of the small secondary cells is reduced to avoid the recirculation zones, which will be unsuitable for the application efficiency. Thus, we notice that the intensity of these small cells is reduced for λ <0.5 (λ=0.4 optimal value), promoting the dominance of the large primary cell. As already explained, the quasi-unicellular flow induced by the RB effect will modify the thermal field distribution according to the counterclockwise convective motion, the isotherms then have a hot quasi-isothermal zone on the right side of the cavity, which will make this ascending particles zone usable in the RB-PCR process by amplifying the denaturation phase; unlike to the regular cavities RB-PCR cases. This improvement is schematically presented in Fig. 9.

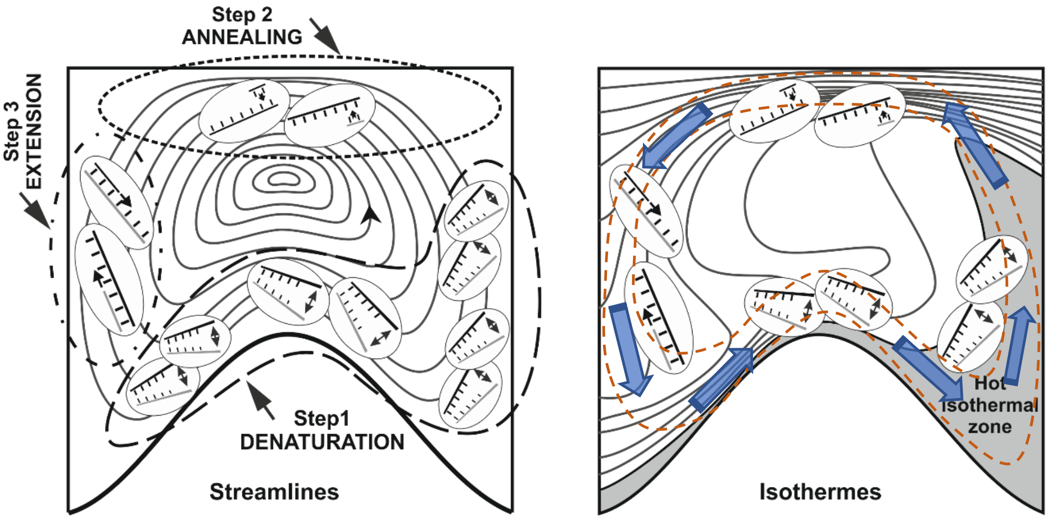

Fig. 9. Schematic PCR in a quasi-unicellular Rayleigh-Bénard flow, Ra=10^{+6}, λ=0.4

On the other hand, we saw overall that the flow intensity is favored in the case of bicellular flow; it is just important to avoid the critical amplitude cases of bifurcation, where the intensity decreases compared to unicellular mode. The great advantage of the bicellular flow remains to double the site of RB-PCR cycle execution (Fig. 10).

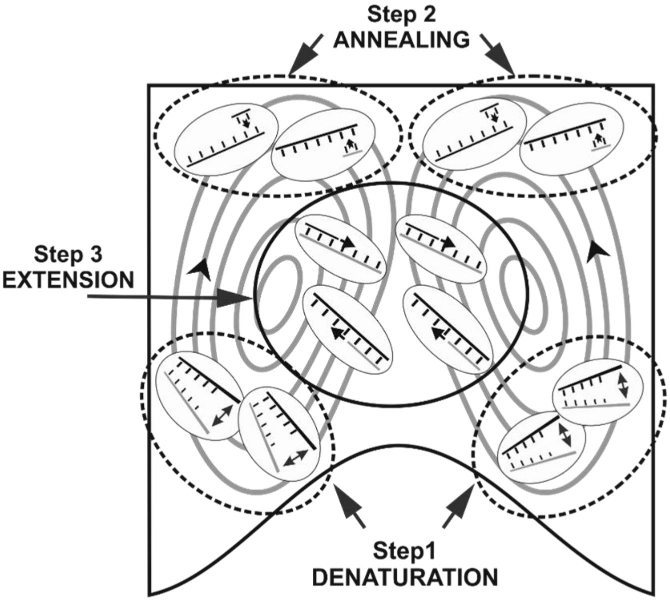

Fig. 10. Schematic PCR in a Bicellular Rayleigh-Benard flow

Through this first analysis, we were able to illustrate the simultaneous effects of the Ra-λ couple on the streamline structures describing the natural convection flow as well as the behavior generated temperature fields. Thus, as a function of the chosen range values, we have given the critical values of the amplitude undulation, as a function of the Rayleigh number, allowing the bifurcation towards the bicellular contra-rotative flow.

Fig. 11 illustrates the variation of the mean Nusselt number as a function of the undulation amplitude and Ra number. For a purely conductive mode ($Ra=10^{+3}$), it can be seen that the average heat exchange is favored with the increasing amplitudes which is due to the increase in the exchange surface. The improvement of the heat transfer compared to the case of a rectilinear wall, represented by dash (N = 0), can exceed 100% for $\lambda \geq 0.4$. In convective mode ($Ra=10^{+4}$ and $Ra=10^{+5}$), as long as the flow regime is unicellular, we find that the average transfer undergoes an increase proportional to the amplitude ($\lambda \leq 0.2$ for $Ra=10^{+4}$ and $\lambda \leq 0.4$ for $Ra=10^{+5}$).

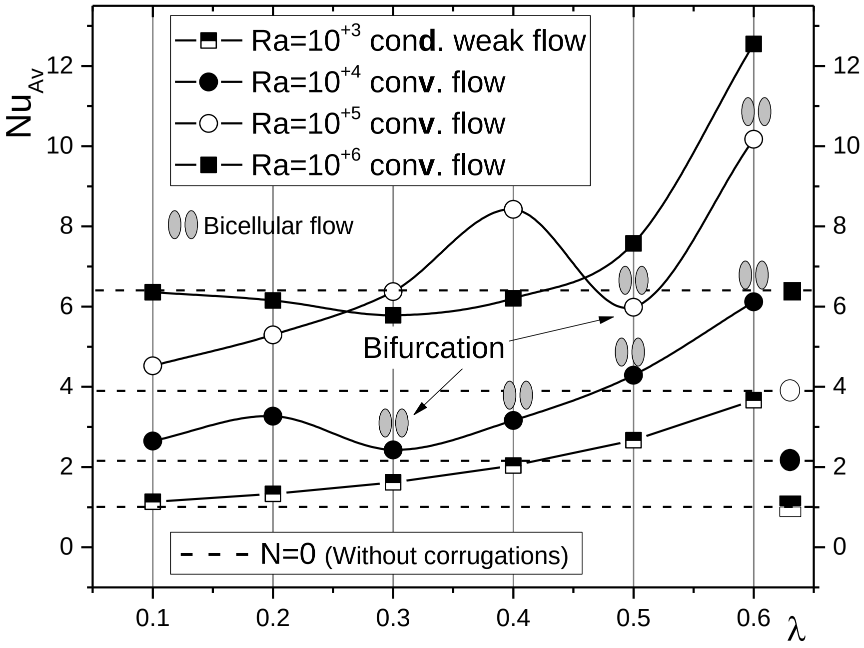

Fig. 11: Average Nusselt as a function of the undulation amplitude and *Ra* number, N=1

As soon as the bifurcation towards bicellular flow is reached, a reduction in the mean Nusselt is observed according to the stabilized redistribution velocity fields, in counter-rotating configuration with expanded thermal boundary layer. The corresponding amplitude values are then described as the critical values (λ_c) allowing the bifurcation towards bicellular regime (*ie*: $\lambda_c=0.3$ for $Ra=10^{+4}$ and $\lambda_c=0.5$ for $Ra=10^{+5}$). Beyond these critical limits, the average heat transfer resumes its increasing evolution with the increase in amplitude, under the significant inertia due to the aggravated confinement. This improved transfer is all the more pronounced as the Ra number is high ($Ra=10^{+5}$). It is important to report the irreversibility bicellular flow installed, which persists with the increasing amplitude, and in any case, we re-observe the unicellular flow. Compared to the regular cavity case (N=0), the average heat transfer recorded with a deformation, presents a considerable improvement, in particular when the thermal force increases (from $Ra=10^{+4}$ to 10^{+5}).

At $Ra=10^{+6}$ we noticed a completely unexpected evolution, where a slight reduction of mean Nusselt is occur for amplitudes 0.1 to 0.4. These Nusselt values are even lower compared to without wavy case (N = 0) found in classical RB convection. Beyond $\lambda=0.4$ the average transfer increase by an exponential growth to reach maximum at $\lambda = 0.6$.

The improvement in heat transfer compared to the case of a regular cavity is represented in Fig. 12, the comparison is described by the ratio between the average Nusselt number calculated as a function of *Ra*-λ and the reference expressed by the average Nusselt number for regular cavity at each *Ra* numbers. These data are shown in Table 1 for the classical RB problem. It is generally observed that the improvement in heat transfer compared to the rectilinear surface increases exponentially with increasing corrugation amplitude for all *Ra* numbers; except at critical amplitudes where the improvement is relatively reduced. For the purely conductive case, the transfer gain with corrugated cavities can reach 900% at λ = 0.8.

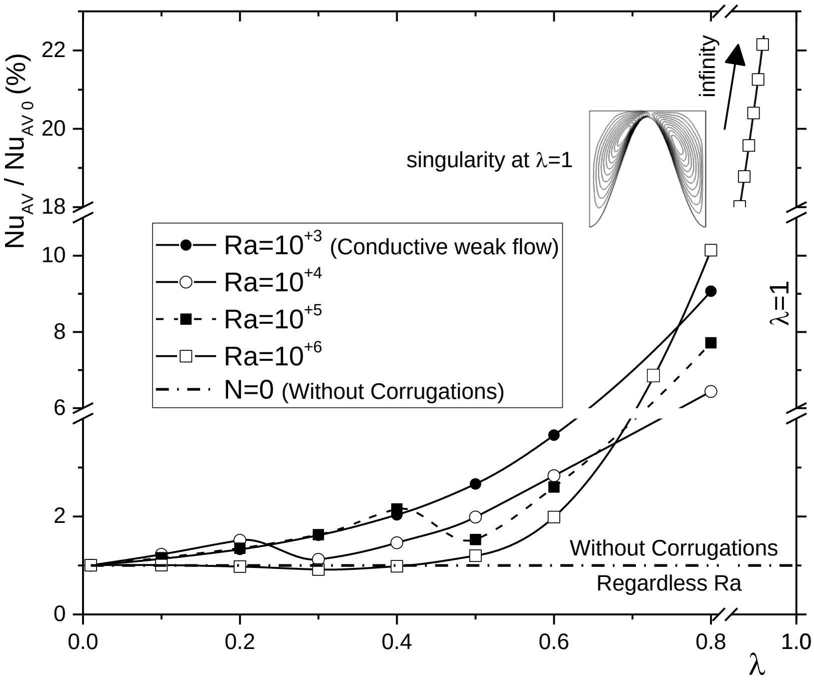

Fig. 12: Relative average Nusselt to RB regular cavity case as a function of the undulation amplitude, N=1

A distinction is noted for *Ra* = 10^{+6} where the gain in transfer increases only from the λ = 0.5, which is due to the isothermal zone induced by deformation. Beyond this value, the convective and geometric effects become cooperative, generating a significant improvement in heat transfer which becomes ten time higher as the flat surface. It should be noted that all the evolutions tend towards an infinite limit value corresponding to the singularity λ = 1.

Fig. 13 summarizes the critical limit of the corrugation amplitudes as a function to Ra number, which affirms the bifurcation towards the bicellular regime and delimits flow patterns according to the *Ra*-λ couple. We note that the value of the critical amplitude λ_c is more important than *Ra* augment, this variation is approximated by correlation valid only for the range of values chosen.

$$\lambda_{crit} = 0.025\ Ra^{0.25} \tag{25}$$

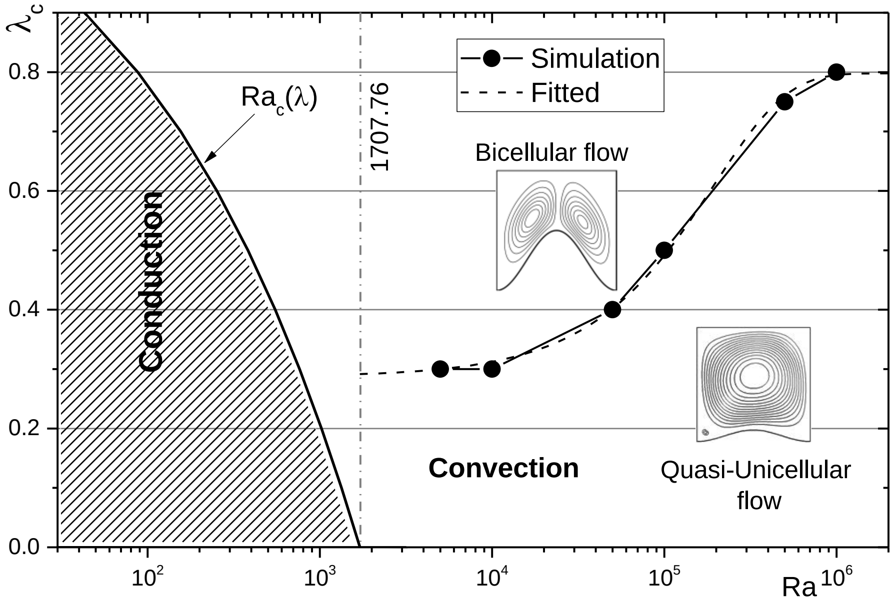

Fig. 13: Critical corrugation amplitudes as a function to *Ra* number, N=1

This behavior suggest that the flow rate controls the bifurcation. The flow rate is the velocity order of magnitude ($Ra^{1/2}$) and the boundary layer size ($Ra^{-1/4}$). To analyze the flow intensity for the different cases of the couple Ra-λ, we represent in Fig. 14 the relative variation of the stream function expressed by the absolute value quantity $(\Psi_{MAX}-\Psi_{MIN}) / \Psi_{MAX}$ which compare the intensity between the primary cell and the secondary cells.

We admit that when Ψ_{MIN} tends towards zero the convective flow tends towards a purely unicellular regime, characterized by a cell circulating counterclockwise and occupying the entire cavity. When Ψ_{MIN} tends towards Ψ_{MAX} we define the perfectly symmetrical bicellular flow. The stream function Ψ_{MIN} then represents, the non-diverging component velocity of the secondary cells whose value is constant, and contrarotative to the primary cell. The relative intensity evolution is thus represented for each *Ra* number as a function of the corrugation amplitude, by simulations and analytical fitted approximations on the same figure. For the sake of clarity, the approximate curves are described in terms of λ/λ_{Crit}, where λ_{Crit} are the bifurcation values corresponding to the bicellular flow birth.

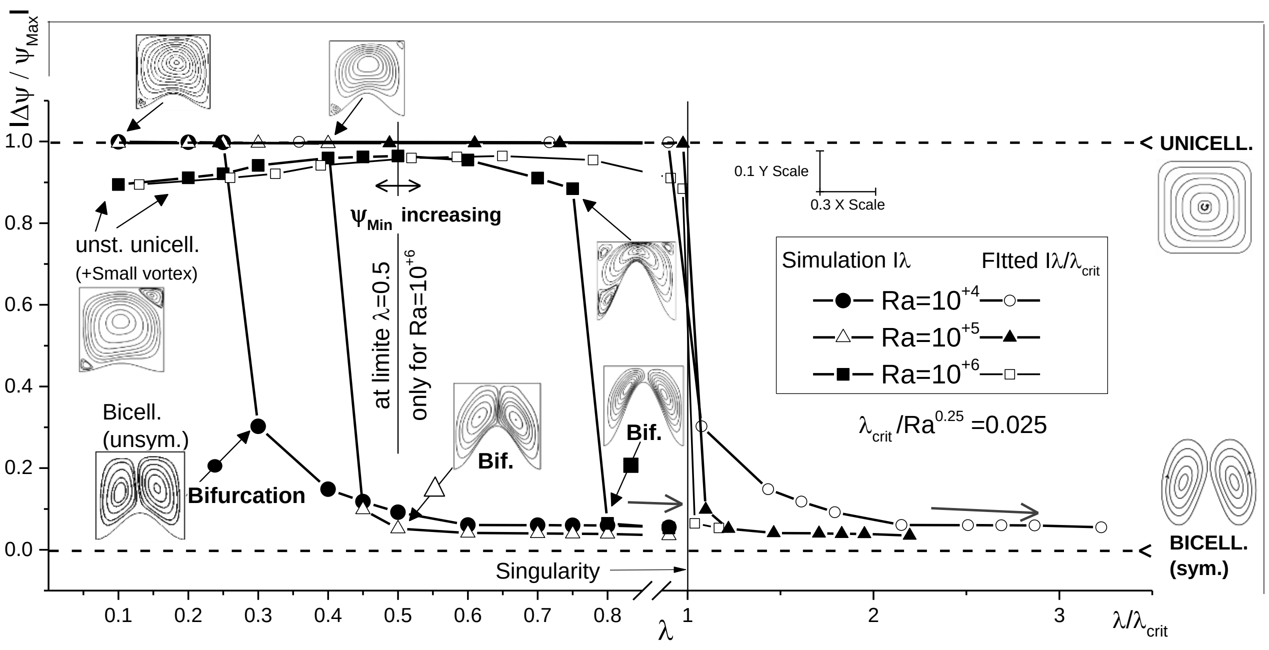

Fig. 14: Relative stream function variation with *Ra*-λ, N=1

For low amplitudes (at Ra=10^{+4} and Ra=10^{+5}), the relative intensity tends towards the unit value indicating the existence of the quasi-unicellular regime dominated by the primary vortex. As the amplitude increases the relative intensity decreases indicating the emergence of secondary cells whose intensity gradually increases. When the geometric bifurcation threshold is reached (λ_{Crit} = 0.3, 0.5, and 0.8 for Ra=10^{+4}, 10^{+5} and 10^{+6} respectively), the unstable bicellular flow settles asymmetrically, and tends towards a symmetrical mode when the geometrical deformation increase. As shown by the fitted curves, it is important to note that the bicellular flow induced at the bifurcation, is all the more symmetrical as the *Ra* number increase, which reduces the slope of the relative intensity while passing from a quasi-unicellular regime towards the bicellular one. Put another way, reducing the effective height (H_{eff} = 1-λ) promotes the orthogonality of the fictitious wall at X=0.5, to improve the convective symmetry between the two counter-rotating cells.

For a large thermal gradient (Ra=10^{+6}) a clear distinction is noted for an effective height greater than 0.5 (*ie*: λ <0.5). Thus, the relative intensity in this case is reversed due to the intensity reduction of the small secondary cells (from λ= 0.1 to λ= 0.4), favoring the dominance of the primary cell. We can therefore conclude that at Ra=10^{+6}, an effective height of the order of 0.5 represents an optimal value for promoting the unicellular regime. We can also show that the critical Ra number as a function of the amplitude λ varies as a function of the effective height $(1-\lambda)^3$.

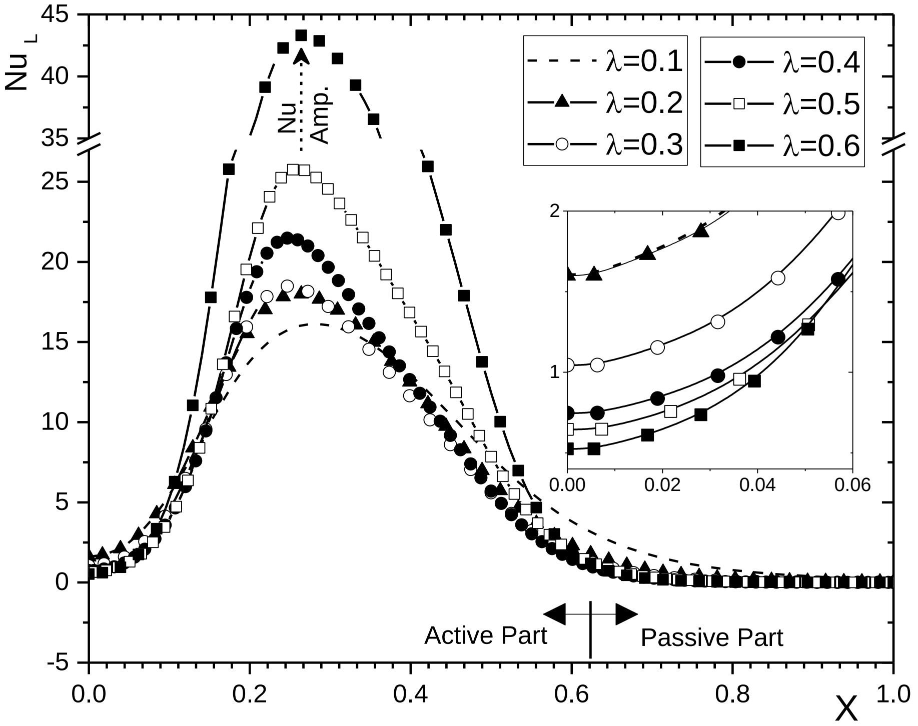

Fig. 15: Local Nusselt numbers long the width of the cavity, $Ra = 10^{+6}$, N=1

The evolutions of the local Nusselt numbers at $Ra = 10^{+6}$ as a function of the width of the cavity are shown in Fig. 15, for the different amplitudes considered. It can be seen that all the curves show an increasing evolution until reaching a maximum value, from which Nu_L is reduced to reach an asymptotic value in the right compartment of the cavity. This value is all closer to zero as the amplitude increases, indicating the adiabatic character of this portion of the lower wall. As already explained, the counterclockwise circular motion, and under the deformation effect, will create an isothermal zone where the thermal gradients will tend towards zero; this portion of the surface is then considered to be totally ineffective for heat transfer, hence our definition of the active and passive parts of the exchange surface. Following flow direction, the parabolic evolutions of the local Nusselt numbers are positioned in the left compartment of the cavity, with an amplitude peak, positioned closer to the left wall as the amplitude deformation increases.

In the bottom left corner of the cavity ($X \leq 0.1$), we notice in Fig. 15 the inversion of the local Nusselt growth order as function of λ (Zoomed part). This phenomenon is justified by the thickening thermal boundary layer in this zone, following the emergence of the small counter-rotating cells exposed in Fig. 8 Thus, the counter-rotating circulation will play a stabilizing role forcing the fluid, in this part, to slow down the dominated primary cell flow, and increasing the thermal gradients in this corner. Therefore, and as these small cells do not appear at low amplitudes, hence this reverse evolution.

To better exploit the local Nusselt variations, we present in Fig. 16 (Ra=10^{+6} and λ=0.6) the different characteristics defining the behavior of Nu_L as a function of the normalized width. We then define the full width at half maximum (**FWHM**) which corresponds to the portion length of wall where the heat exchange will double to reach its maximum value. The heat transfer centroid is also defined as the position around which the heat transfer takes place, with maximum crushing of the thermal layer. The notion of the active and passive wall portions will allow us to define the dimension of the passive surface on which the wall is almost adiabatic with an almost zero transfer, and vice versa, the active portion where the transfer takes place. The limit position between these two portions is represented by the position X_A on the dimensionless scale. To determine this position, we assumed that the heat transfer is considered adiabatic, when the local Nusselt number is less than 1% of the maximum value recorded at the peak of its parabolic variation (ie: Nu_L (X_A) = 1% $Nu_{L\ MAX}$).

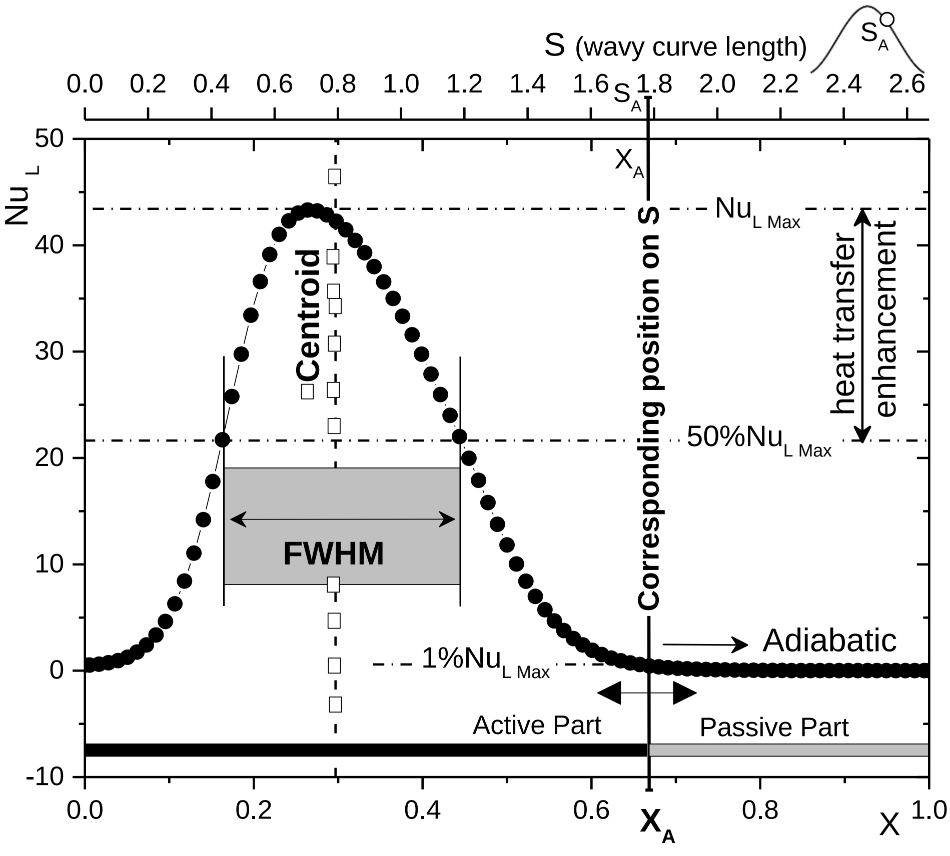

Fig. 16: Characteristics defining local Nusselt number, *Ra* = 10^{+6}, λ=0.6, N=1

The normalized position X_A will correspond to the position SA on the real scale (S (λ)) which represents the total length of the deformation curvature already defined in the calculation of the local Nusselt number. This position couple (X_A, S_A) will tell us about the normalized and real positions delimiting the passive portions to the variation of thermal gradients.

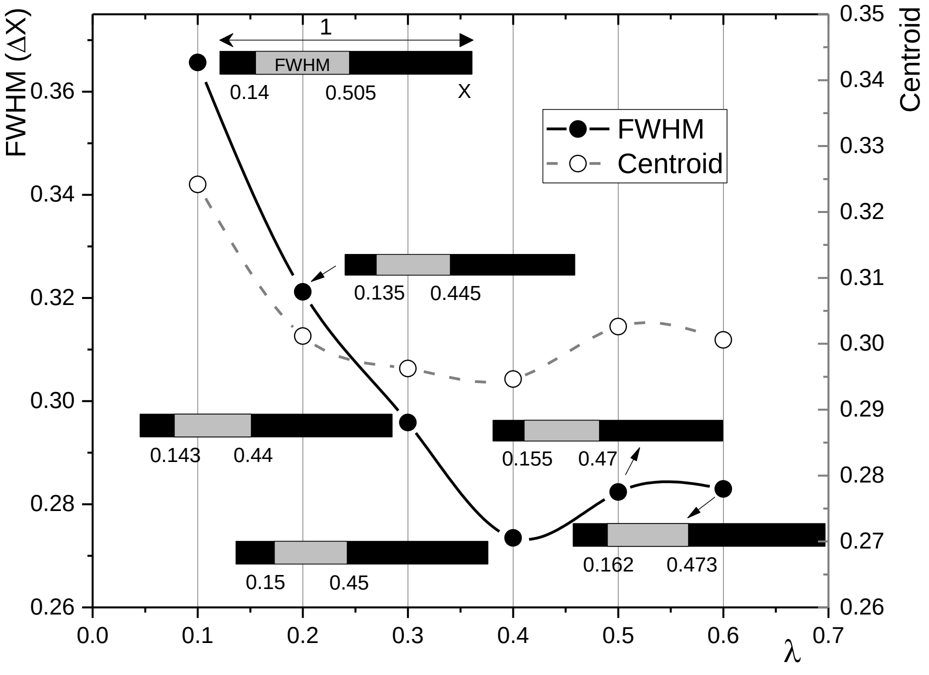

Fig. 17: The FWHM and centroid of heat transfers for different amplitude, *Ra* = 10^{+6}, N=1

Fig. 17 represents the FWHM variations and those of the centroid of the transfers for the different undulation amplitudes. We note that FWHM does not vary too much; nevertheless, we notice its reduction for λ≤0.4, which reduces the dimension of the maximum transfer. However, the FWHM for λ≥0.5 increases slightly and improves the area under the curve. Heat transfer centroid is generally around the position X = 0.3, with tendency to approach the left wall for the λ≤0.4.

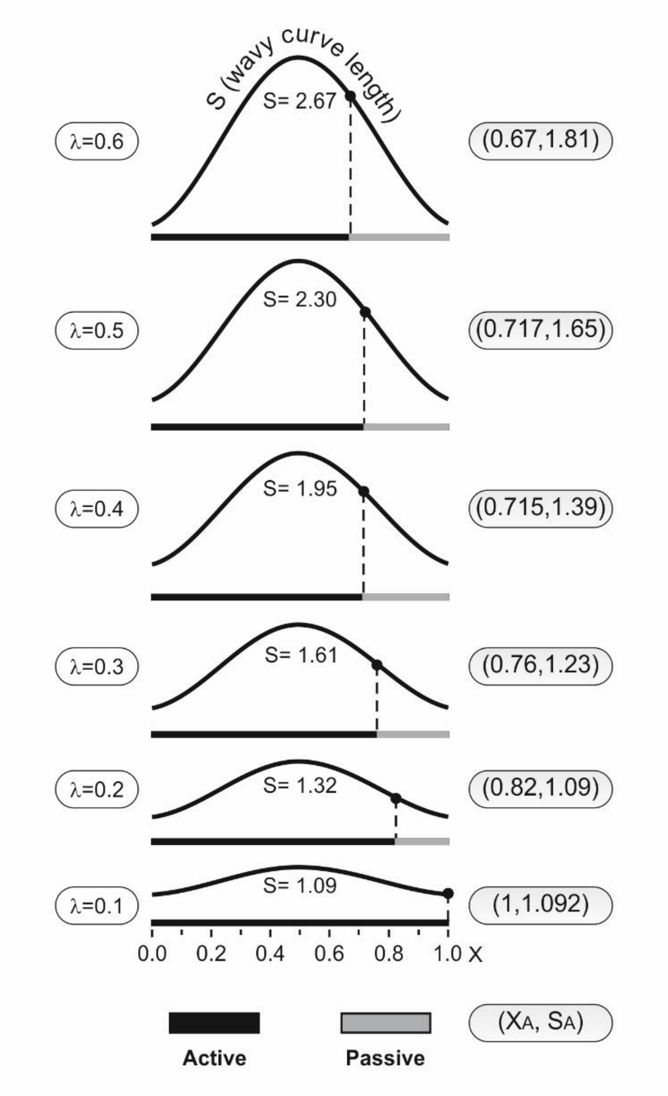

Fig. 18: Positions delimiting the passive and active portions, *Ra* = 10^{+6}, N=1

Fig. 18 summarizes the different positions of the couple (X_A, S_A) delimiting the passive portion of the active part of the total heat transfer surface, at *Ra* = 10^{+6}. We note for $\lambda = 0.1$, that the entire wall surface is active to the heat transfer process; whereas, for amplitudes 0.2 to 0.4, the length of passive portion is as all as more important, which reduces the heat transfer efficiency and justifies the average quantities represented in figure 8. This analysis cannot be based solely on the geometrical aspect, but it is necessary to associate the physical character; because for example at $\lambda = 0.6$, we notice that the passive part is the most important despite that the average transfer is the highest. Thus, the effect of the aggravated confinement will induce a significant intensification flow and consequently thinner thermal boundary layers. This will compensate loss due to the passive portion.

For RB-PCR process, a larger passive part favors the denaturation stage, which increases the amplification efficiency.

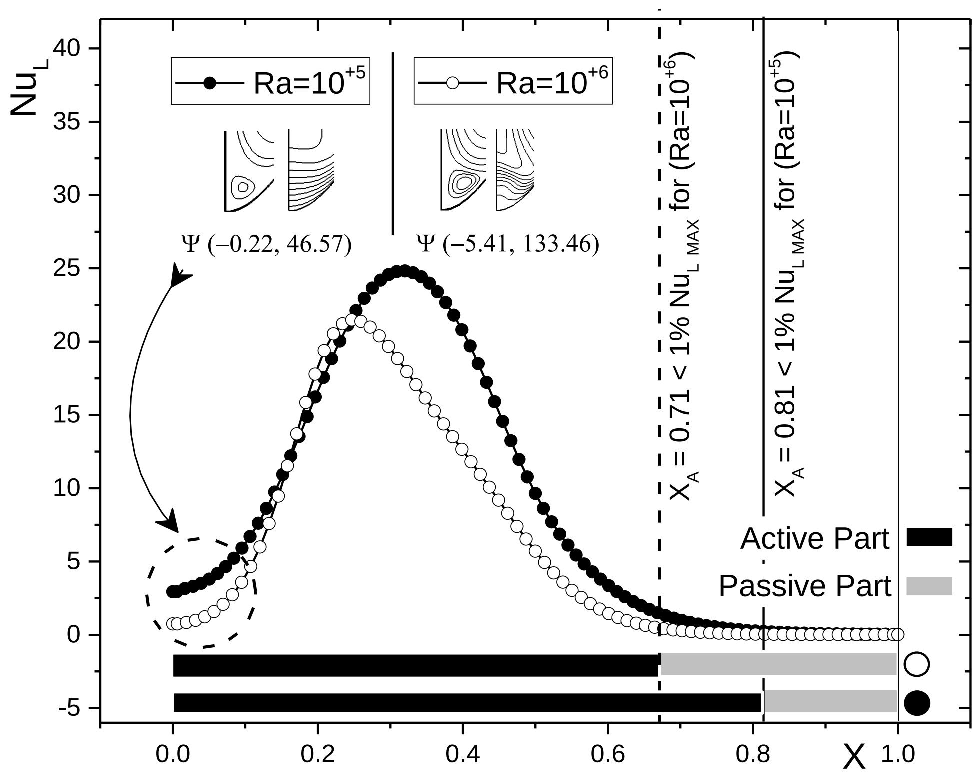

Fig. 19: Comparison of the local Nusselt Number evolutions for
Ra = 10^{+6} and *Ra* = 10^{+5}, $\lambda = 0.4$, N=1

To justify that the average exchange recorded at *Ra*=10^{+5} is more important than that of *Ra*=10^{+6}, for the same amplitude (λ=0.4), we present on Fig. 19 the local Nusselt number behaviors in function of X. It is clearly noted that the passive portion length is greater for the case of *Ra*=10^{+6} (X_A=0.7) than *Ra*=10^{+5} (X_A=0.8); which reduces the exchange efficiency for the first case. On the other hand, the birth of small cells at left corners of the cavity, already mentioned in Fig. 10, and due to the counter-rotating and high fluid circulation, the thermal boundary layer will thicken reducing the thermal gradients in this transfer zone, and therefore reducing the average Nusselt number. This is clearly shown by the portions streamlines and isotherms shown in Figure 18. Under the effect of these two aspects, it is obvious that the area under the local Nusselt curve at *Ra*=10^{+6} is reduced.

To complete our analysis of the heat transfer behavior and fluid flow structures, we have represented a cartography, on a logarithmic scale, which summarizes the variation of Iso-

Nusselt as a function of the couple *Ra*-λ (Fig .20). Overall, this figure shows that the heat transfer is favored by increasing the two control parameters, with a distinction for the case of *Ra*=10^{+6}. The disturbance recorded in the vicinity of *Ra*=10^{+6} is essentially due to the behavior of the secondary convective cells on both sides of the effective optimal height H_{eff} = 0.5.

The figure delimits the bifurcation line from the primary quasi-unicellular regime towards the secondary bicellular flow, under the interaction constraint of the geometric effects, due to the deformation, to those of thermal origin.

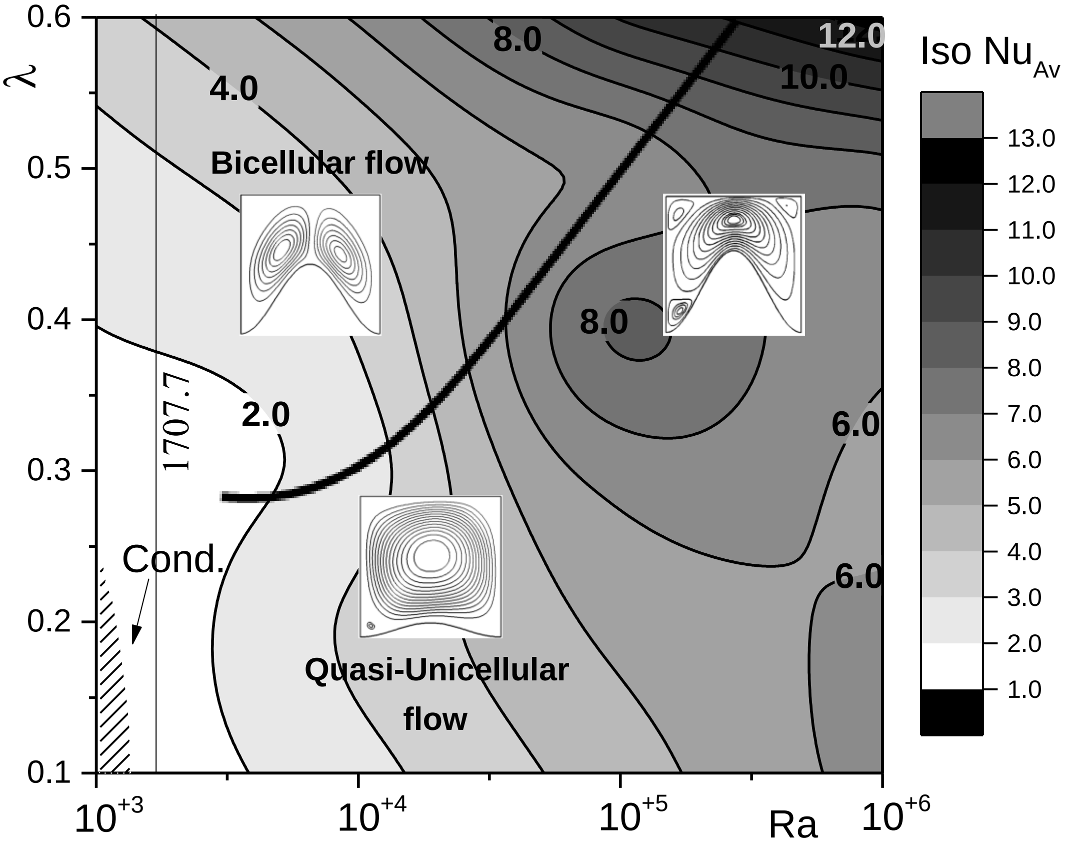

Fig. 20: Iso Nusselt as a function of the Ra-l couple, λ = 0.4, N=1

5. Conclusion

Natural convection heat transfer in a corrugated cavity filled with fluid heated from below is studied numerically. The bottom surface is considered to follow a wavy pattern. Results analysis focused on the influence of the different controlling parameters derived from the dimensionless mathematical model, and which describe the thermophysical and geometrical effects induced in the corrugated enclosure. The flow intensity and structure were anlysed for mastering the engineering Polymerase chain reaction (PCR) process.

For the considered domain, beyond the convective instability threshold, we have demonstrated the existence of a bifurcation from quasi-unicellular flow towards a bicellular regime, controlled exclusively by corrugations amplitude value. An approximate solution has been proposed to these critical amplitude values (λ_c), depending on Rayleigh number. For bicellular convective regime, the isotherms present quasi-symmetrical distortions relative to the center line X = 0.5.

An optimal configuration, for wavy cavity with an amplitude of 0.4 ($Ra=10^{+5}$), was found to promote the amplification of DNA sample by RB-PCR. This optimum is due to the reduction of the recirculation zones caused by secondary cells and a quasi-unicellular regime. Moreover, we identified the forming of isothermal zone between the vicinity of the vertical cavity wall and the demonstrated passive heat transfer lower zone. Such isothermal active zone will be used to amplify the denaturation phase of the PCR process to improve the amplification. Recall that this upward flow zone was completely inactive in the case of a regular cavity. Such isothermal zone, under the critical amplitude value ($\lambda_c=0.8$ at $Ra=10^{+6}$), is of the size of λ due to the thermal boundary layer behavior,.

For the bifurcation case towards the bicellular flow, a small effective height ($\lambda \rightarrow 1$) ensures a great intensity of flow which improves the efficiency of the RB-PCR protocol, without forgetting the fact of doubling the execution site of amplification. For heat exchanges, this configuration significantly improves heat transfer compared to the regular cavity.

The behavior of the secondary cells and their influences on the thermal boundary layer, proved significant difference between the cases $Ra=10^{+5}$ and $Ra=10^{+6}$. This induced difference effect is due to the geometric deformation, and against all expectations, gives a higher average heat exchange at $Ra=10^{+5}$ than 10^{+6}.

Finally, an interesting cartography summarizing the Iso-Nusselt distribution as a function of the *Ra*-λ couple is presented. This map summarise also the flow topologies and bifurcations.

As a perspective to this work, we plan to explore other optimization based on the control parameters, notably the corrugation number. To better understand and predict the behavior of the fluid flow as well as the heat transfer modes and their efficiencies related to the PCR an integration of the chain forming kinetics versus the temperature and the local concentration is also required.

Aknowledgments

The authors acknowledge with thanks Ms. S. Mimouni from the Biological laboratory for the scientific exchanges and visit of the process apparatus.

References

[1] Y. Varol, Hakan F. Oztop, Free convection in a shallow wavy enclosure, Int.Com.. Heat and Mass Transfer 33, (2006) 764-771.

[2] S. Saha, T. Sultana, G. Saha, M.M. Rahman, Effects of discrete iso flux heat source size and angle of inclination on natural convection heat transfer flow inside a sinusoidal corrugated enclosure, Int. Com.in Heat and Mass Transfer 35, (2008) 1288–1296.

[3] S. Mahmud, P.K. Das, N. Hyder, A.K.M.S. Islam, Free convection in an enclosure with vertical wavy walls, Int. J. Therm. Sci. 41 (2002) 440–446.

[4] P.K. Das, S. Mahmud, Numerical investigation of natural convection inside a wavy enclosure, Int. J. Therm. Sci. 42 (2003) 397–406.

[5] P.K. Das, S. Mahmud, H. Tasnim, A. Sadrul, Effect of surface waviness and aspect ratio on heat transfer inside a wavy enclosure, Int. J. of Numerical Methods for Heat & Fluid Flow Vol. 13 No. 8, (2003) 1097-1122.

[6] B. Favier, J. Purseed, L. Duchemin, Rayleigh-Bénard convection with a melting boundary, J. of Fluid Mechanics, 858, (2019) 437-473.

[7] A.S. Gawas, D.V. Patil, Rayleigh-Bénard type natural convection heat transfer in two-dimensional geometries, Applied Thermal Engineering 153 (2019) 543–555.

[8] M. Bisht, S. Haeri, D. V. Patil, Fluid flow in wall-driven enclosures with corrugated bottom, Computers and Fluids 152 (2017) 1–13.

[9] D. Mouhtadi, A. Amahmid, M. Hasnaoui,R. Bennacer, Natural convection in a horizontal channel provided with heat generating blocks: Discussion of the isothermal blocks validity, Energy Conversion and Management, 53, Issue 1, (2012), 45-54.

[10] O. Rahli, R. Bennacer, K. Bouhadef, D. E. Ameziani, Three-Dimensional Mixed Convection Heat and Mass Transfer in a Rectangular Duct: Case of Longitudinal Rolls, Numerical Heat Transfer, Part A59: 5, (2011), 349- 371, DOI:10.1080/10407782.2011.549081.

[11] L. Adjlout, O. Imine, A. Azzi, M. Belkadi, Laminar natural convection in an inclined cavity with a wavy wall, Int. J. Heat Mass Transfer 45, (2002) 2141–2152.

[12] P. Biswal, T. Basak, Role of differential vs Rayleigh-Bénard heating at curved walls for efficient processing via entropy generation approach, International Journal of Heat and Mass Transfer 124 (2018) 390–413.

[13] K. Choukairy, R. Bennacer, P. Vasseur, Natural convection in a vertical annulus boarded by an inner wall of finite thickness, Int. Coo. Heat Mass Transfer, Vol 31, N°4 (2004), 501-512.

[14] A. Misirlioglu, A. C. Baytas, I. Pop, Free convection in a wavy cavity filled with a porous medium, International Journal of Heat and Mass Transfer 48 (2005) 1840–1850.

[15] S. H. Hussain, A. K. Hussein, M. M. Mahdi, Natural convection in a square inclined enclosure with vee-corrugated sidewalls subjected to constant flux heating from below, Nonlinear Analysis: Modelling and Control, Vol. 16, No. 2, (2011) 152–169.

[16] A.Chattopadhyay, S. K. Pandit, H. F. Oztop, An analysis of thermal performance and entropy generation in a wavy enclosure with moving walls, European Journal of Mechanics / B Fluids 79 (2020) 12–26.

[17] T. Nolan, R.E. Hands, S.A. Bustin, Quantification of mRNA using real-time RTPCR, Nat. Protoc. 1 (2006) 1559-1582.

[18] M.J. Espy, J.R. Uhl, L.M. Sloan, S.P. Buckwalter, M.F. Jones, E.A. Vetter, J.D. Yao,N.L. Wengenack, J.E. Rosenblatt, F.R. Cockerill, Real-time PCR in clinical microbiology: applications for routine laboratory testing, Clin. Microbiol. 19 (2006) 165-256.

[19] G. Miao, L.Zhang, J. Zhang, S. Ge, N. Xia, S.Qian, D. Yu, X. Qiu, Free convective PCR: From principle study to commercial applications - A critical review, Analytica Chemica Acta 1108 (2020) 177-197.

[20] Yu Huang, Kashan Memon, S.M. Chapal Hossain, Ji Peng, Jianye Wang, Zhiquan Shu, Kui Ma, Lingxiao Shen, Frank Liu Gao, Yunxia Cao, Peng Hu, Gang Zhao, Heat transfer analysis of a self-designed cooling rate controllable device and its application for cryopreservation of biological cells, Applied Thermal Engineering 148 (2019) 768–776.

[21] J. Shi, Z.Q. Chen *, M.H. Shi, Simulation of heat transfer of biological tissue during cryosurgery based on vascular trees, Applied Thermal Engineering 29 (2009) 1792–1798.

[22] K.J. Chua, S.K. Chou, On the study of the freeze–thaw thermal process of a biological system, Applied Thermal Engineering 29 (2009) 3696–3709.

[23] J. J. Chen, I. H. Hsieh, Using an IR lamp to perform DNA amplifications on an oscillatory thermocycler, Applied Thermal Engineering 106 (2016) 1–12.

[24] Z. Li, Y. Zhao, D. Zhang, S. Zhuang, Y. Yamaguchi, The development of a portable buoyancy-driven PCR system and its evaluation by capillary electrophoresis, Sensors and Actuators B 230 (2016) 779–784

[25] E. Yariv, G. Ben-Dov, K. D. Dorfman, Polymerase chain reaction in natural convection systems: A convection-diffusion-reaction model, Europhys. Lett., 71 (6), (2005) 1008–1014.

[26] W. Benett, F. Milanovich, J. Richards, Convectively Driven PCR Thermal-Cycling, (2003). US 6,586,233 B2.

[27] H.J. Hwang, J.H. Kim, K. Jeong, Method and Apparatus for Amplification of Nucleic Acid Sequences by Using Thermal Convection, (2003). WO 03/025226.

[28] Z. Li, The development of a portable buoyancy-driven PCR system and its evaluation by capillary electrophoresis, Sensor. Actuator. B Chem. 230 (2016) 779-784.

[29] J.F. Thompson, Z.U.A. Warsi, C.W. Mastin, Numerical Grid Generation, North Holland, (1985).

[30] D. Anderson , J. Tannehill, R. Pletcher. Computational Fluid and Heat Transfer, Mc Graw Hill, (1984).

[31] J.D. Anderson , Computational Fluid Dynamics : The Basic with Applications, Int. Editions, Mc Graw Hill, (1995).

[32] S.V. Patankar. Numerical Heat transfer and Fluid Flow. Mc Graw Hill, (1980).

[33] B. P. Leonard, “A stable and accurate convective modeling procedure based on quadratic upstream interpolation,” Comp. Meth. Appl. Mech. Engineering **19**, 59 (1979).

[34] N. Ouertatani, N.Ben Cheikh, B. Ben Beya, T. Lili, Numerical simulation of two-dimensional Rayleigh–Bénard convection in an enclosure, C. R. Mecanique 336, (2008) 464–470.

Nomenclature

Latin letters

a	Thermal diffusivity
Cp	Heat capacity
H	Height / Length
J	Jacobian
k	Thermal conductivity
K	Permeability
$\hat{n}$	Unit normal vector
N	Corrugations number
Nu	Nusselt number
P	Dimensionless pressure
Pr	Prandtl number
Ra	Rayleigh number
S	Curve length
T	Temperature
u, v	Velocity component (x,y)
U, V	Dimensionless Velocity (X, Y)
U^c, V^c	Contravariant velocity (ξ , η)
x, y	Coordinates
X, Y	Dimensionless coordinates

Greek

μ	Dynamic viscosity
ρ	Fluid density
θ	Dimensionless temperature
ξ , η	Curvilinear coordinates.
ν	Fluid kinematic viscosity
λ	Corrugation amplitude
Ψ	Stream function

Subscripts

A	Active
Av	Average
c	Cold / Critical
eff	effective
h	Hot
L	Local
MAX	Maximum
MIN	Minimum